

Effects of yawed inflow on the aerodynamic and aeroacoustic performance of ducted wind turbines

Dighe, Vinit V.; Avallone, Francesco; van Bussel, Gerard

DOI

[10.1016/j.jweia.2020.104174](https://doi.org/10.1016/j.jweia.2020.104174)

Publication date

2020

Document Version

Final published version

Published in

Journal of Wind Engineering and Industrial Aerodynamics

Citation (APA)

Dighe, V. V., Avallone, F., & van Bussel, G. (2020). Effects of yawed inflow on the aerodynamic and aeroacoustic performance of ducted wind turbines. *Journal of Wind Engineering and Industrial Aerodynamics*, 201, Article 104174. <https://doi.org/10.1016/j.jweia.2020.104174>

Important note

To cite this publication, please use the final published version (if applicable). Please check the document version above.

Copyright

Other than for strictly personal use, it is not permitted to download, forward or distribute the text or part of it, without the consent of the author(s) and/or copyright holder(s), unless the work is under an open content license such as Creative Commons.

Takedown policy

Please contact us and provide details if you believe this document breaches copyrights. We will remove access to the work immediately and investigate your claim.



Effects of yawed inflow on the aerodynamic and aeroacoustic performance of ducted wind turbines

Vinit V. Dighe^{*}, Francesco Avallone, Gerard van Bussel

Wind Energy Research Group, Faculty of Aerospace Engineering, TU Delft, Netherlands

ARTICLE INFO

Keywords:

Ducted wind turbine
CFD
Aerodynamics
Aeroacoustics

ABSTRACT

Ducted Wind Turbines (DWTs) can be used for energy harvesting in urban areas where non-uniform inflows might be the cause of aerodynamic and acoustic performance degradation. For this reason, an aerodynamic and aeroacoustic analysis of DWTs in yawed inflow condition is performed for two duct geometries: a baseline commercial DWT model, DonQi®, and one with a duct having a higher cross-section camber with respect to the baseline, named DonQi D5. The latter has been obtained from a previous optimization study. A numerical investigation using Lattice-Boltzmann Very-Large-Eddy Simulations is presented. Data confirm that the aerodynamic performance improvement, i.e. increase of the power coefficient, is proportional to the increase of the duct thrust force coefficient. It is found that, placing the DWT at a yaw angle of 7.5°, the aerodynamic performances of the DonQi D5 DWT model are less affected by the yaw angle. On the other hand, this configuration shows an increase of broadband noise with respect to the baseline DonQi® one, both in non-yawed and yawed inflow conditions. This is associated to turbulent boundary layer trailing edge noise due to the turbulent flow structures developing along the surface of the duct.

1. Introduction

The European Union (EU) aims at reducing greenhouse gas emissions to 80–95% below 1990 levels by 2050 (Barthelmie and Pryor, 2014). To meet EU 2050 energy targets, exploitation of the full potential of wind energy is needed, not only offshore, but also onshore. A possible solution to increase the energy produced onshore is to use small wind turbines that can be located close to urban environments (Fogaing et al., 2019). Integration of wind turbines into urban environments is challenging because of lower wind speed, non-uniform inflow and larger turbulent fluctuations compared to free field caused by the presence of buildings that act as distributed roughness elements. To address these challenges, design modifications of urban wind turbines are required.

A possible technological solution to extract wind energy in urban areas is represented by Ducted Wind Turbines (DWTs). DWTs increase the energy extraction with respect to conventional horizontal axis wind turbines (HAWTs) for a given turbine radius and free-stream velocity (van Bussel, 2007). DWTs are constituted of a turbine and a duct (also named as diffuser or shroud); the role of the latter is to increase the mass-flow through the turbine relative to a similar turbine operating in the open atmosphere, thereby increasing the generated power. The

working principle, as explained by de Vries (1979), is that if the sectional lift force of the duct is directed towards the axis of rotation, then the associated circulation induces an increased mass flow through the turbine (see Fig. 1).

The first in depth analysis of the DWT concept was performed by Lilley and Rainbird (1956) using one dimensional momentum and vortex theories. Their analysis suggested that a DWT can gain 65% in the power output in comparison to a bare wind turbine with the same turbine radius. They showed that, for a DWT, the gain in the power output is due to the increase in the axial velocity across the turbine and the reduction of turbine tip-losses.

Later, Kogan and Nissim (1962), Kogan and Seginer (1963), and Igra (1976, 1977, 1981) investigated the DWT concept using one dimensional momentum theory and a series of experiments with an actuator disc (AD) model to represent the turbine. They concluded that the power augmentation factor, which is the ratio of the power output for a DWT to that of a bare wind turbine, is dependent on the thrust generated by the duct, the duct exit-area-ratio and the duct's static pressure recovery. They were the first to report that the sub-atmospheric pressure at the duct exit plane affects DWTs aerodynamic performance. In the second phase of experiments, a compact version of the initial duct was investigated. In

^{*} Corresponding author.

E-mail address: v.v.dighe@tudelft.nl (V.V. Dighe).

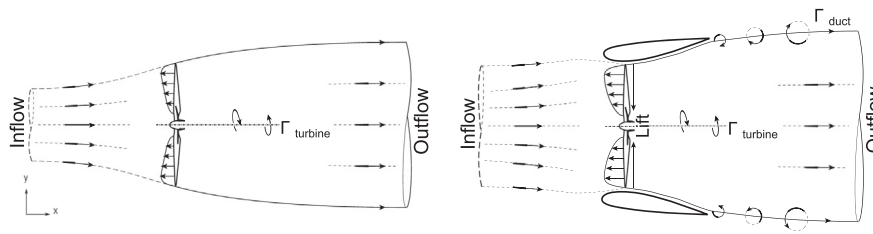


Fig. 1. Schematic of stream-tube model for a bare wind turbine (left) and DWT (right). The bound circulation from the wind turbine blades and the duct surface is denoted by Γ .

order to increase the duct exit-area-ratio, three ring-shaped flaps were placed at the duct exit. With this setup, the overall length-to-diameter was nearly halved whilst maintaining the power augmentation factor of approximately 2.8. The third phase witnessed a complete change of the duct and flap geometry; the cross-section profiles were derived from NACA airfoils. Igra found that the addition of airfoil-shaped flap improves the DWTs aerodynamic performance by 25% when compared to a single duct configuration.

Following Igra's work, Gilbert and Foreman (1983) from Grumman Aerospace Corporation addressed the key issue for DWTs success: the cost reduction of the duct. Goal of the research was to reduce the size of the duct, thereby reducing the manufacturing cost whilst maintaining its performance. Grumman researchers identified the use of boundary layer control technique to manufacture compact ducts with a large exit-area-ratio. Adopting this technique, flow separation delay was achieved by re-energizing the boundary layer flow along the inner walls of the duct, thus improving the overall performance. The optimal design for the baseline geometry was determined through a parametric study of duct exit-area-ratio, number of boundary layer slots, their position, size and geometry, as well as center-body configuration (Foreman and Gilbert, 1984). The performance benefits, however, did not match the high costs incurred in the implementation of the flow control technology.

In the 1990s, Vortec, a New Zealand company attempted to commercialize a DWT design (Phillips et al., 1999). The design was studied using wind tunnel experiments and Reynolds Averaged Navier Stokes (RANS) simulations. The project was abandoned when their 7 m prototype did not perform as well as expected. The Vortec turbine design required heavy support structures to withstand the high turbulent flow in storm conditions. Additionally, the power predicted by the RANS simulations was significantly higher than that reached in the test conditions (Phillips et al., 2008).

Literature on DWT was sparse until 2000s when Hansen et al. (2000) studied DWTs performance with a RANS approach. They proved that the power augmentation factor for a DWT is proportional to the increased mass flow through the turbine, and not with the cube of the increased turbine plane velocity. van Bussel (2007) developed an Axial Momentum Theory (AMT) for DWTs analogous with the AMT for bare wind turbines. He compared the results of his theory with the numerical predictions obtained by Hansen et al. (2000), and also provided an extensive review and comparison with the experimental data available from Igra (1981), Gilbert and Foreman (1983) and Phillips et al. (1999). The conclusions of van Bussel were that the amount of energy extraction for a DWT is identical to that of a bare wind turbine, and a significant power augmentation for a DWT can be obtained with a strong reduction of the static pressure at the duct exit. Similar conclusions were obtained by Werle and Presz, (2009) and Jamieson and Hassan (2011).

During the last decade, there is a renewed interest in the DWT research using numerical methods. Widnall (2009) proposed a potential-flow vortex method to analyze the incompressible flow field past a DWT. This method assumes a uniform change in the static and stagnation pressure across the AD under the influence of an axisymmetric duct represented using vortex panels. Afterwards, Bontempo and Manna (2013) developed a semi-analytical method to evaluate the performance of the DWT for a prescribed turbine load distribution and duct geometry.

Unlike the potential-flow vortex method proposed by Widnall (2009), the semi-analytical method by Bontempo and Manna (2013) takes into account the wake rotation and divergence. Due to the inviscid nature of the solutions, the methods can only handle ducts of general shapes without high camber and thickness distribution. More recently, De Oliveira et al. (2016), using a potential-flow vortex method, confirmed that embedding a turbine within a duct improves the DWTs performance; the improvement, however, depends on the duct geometry. In order to include the viscous effects and the duct geometry on the DWT performance, Dighe et al. (2019a) carried a two-dimensional study on duct shape parameterization using RANS simulations. They found that increasing the duct cross-section camber improves the aerodynamic performance of the DWT until separation occurs inside the duct. They concluded that inner duct wall flow separation reduces the aerodynamic performance of DWT. This has also been confirmed by the more recent three-dimensional simulations performed by Avallone et al. (2020).

In reviewing the research on DWTs to date, it can be concluded that ducts can improve the power production of wind turbines in an unbounded flow. Despite the numerous theoretical, numerical and experimental investigations, the full potential benefits of the DWT concept has not yet been investigated focusing on the flow physics of a more realistic configuration (van Bussel, 2015). As a matter of fact, focusing on numerical simulations, most of them were performed by representing the turbine by a simplified AD model with an imposed pressure jump. Due to the complex aerodynamic interactions between the duct and the turbine, it is necessary to include aspects such as non-uniform blade loading, wake swirling and unsteady flow fluctuations. In addition, it is expected that DWTs will work in off-design conditions, because of their installation in complex urban environment. For these reasons, three-dimensional Lattice-Boltzmann Very Large Eddy Simulations (LB-VLES) of DWTs, where the rotor is simulated, in axial and yawed inflow conditions are presented in this paper. The additional effects of inflow turbulence intensity are neglected for the sake of simplicity. The analysis is further complemented with far-field noise analysis because the installation of DWTs in urban areas is subject to noise regulations laid by the local authorities. It is worth mentioning that, even in the absence of a dedicated study, researchers have contrasting opinions on the noise produced by a DWT (Lubitz and Shomer, 2014; Ohya and Karasudani, 2010; Takahashi et al., 2012). This study will provide explanations on this matter as well.

The rest of the paper is organized as follows. Section 2 describes the numerical methodology adopted for the aerodynamic and aeroacoustic calculations. Section 3 details the geometric parameters of the DWT models chosen and the numerical setup for the LB-VLES. Section 4 reports the verification and validation study. Flow field analysis is presented in section 5. Insights on the aerodynamic and aeroacoustic performance coefficients for two DWT models, both under non-yawed and yawed inflow conditions, are discussed in sections 6 and 7, respectively. The most relevant results are summarized in the conclusions.

2. Numerical methodology

The CFD solver Simulia PowerFLOW® 5.4a based on the Lattice-Boltzmann method (LBM) is used to calculate the unsteady flow around

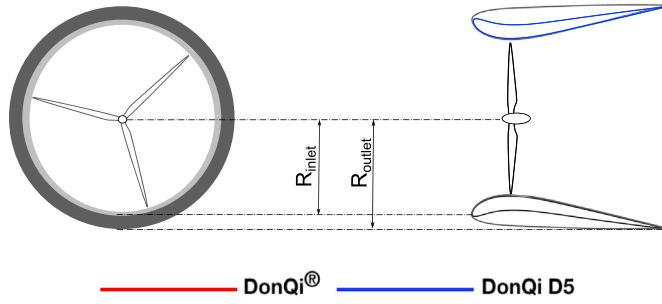


Fig. 2. Front view of the DWT models (left) with the cross-section view detailing the geometric parameters of the two duct profiles (right).

the DWT models. The solver has been validated for aerodynamic and aeroacoustic analysis for a similar class of problems (Avallone et al., 2018, 2020).

The software solves the LB equations for a finite number of directions. LB equations, by nature, are explicit, transient and compressible. For a detailed description, the reader can refer to Chen and Doolen (1998a) and Succi (2001). For an incompressible fluid in isothermal conditions, the Navier Stokes equations can be derived from the LB equations (Shan et al., 2006). Statistically, the LB equations describe the particle motion at a position x in the i -th direction at time t . The macroscopic flow variables, such as density and velocity, are determined by taking summation over the set of discrete directions of the particle distribution function. The particle distribution function $\Omega(f)$ is solved by means of the Boltzmann equation on a mesh composed of cubic volumetric elements (voxels) and surface elements (surfels), known as lattice. A Very Large Eddy Simulation (VLES) model is implemented to take into account the unresolved scales of turbulence. A two equation $k - \varepsilon$ Renormalization Group (RNG) is used to compute the turbulent relaxation time that is added to the viscous relaxation time.

A pressure-gradient-extended wall-model (PGE-WM) is used to approximate the no-slip boundary condition on solid walls (Teixeira, 1998). The model is based on the extension of the generalized law-of-the-wall model (Lauder and Sharma, 1974) to take into account the effect of pressure gradient, given by the following analytical expression:

$$u^+ = \frac{1}{k} \ln\left(\frac{y^+}{A}\right) + B \quad (1)$$

where u^+ and y^+ are the boundary-layer velocity and the non-dimensional wall distance, respectively, $k = 0.41$ is the von Karman constant and $B = 5.2$ is the log-law constant. A is a function of pressure gradient. It captures the physical consequence that the velocity profile slows down and so expands, due to the presence of the pressure gradient, at least at the early stage of the development. The expression for A is:

$$A = 1 + \frac{f \left| \frac{dp}{ds} \right|}{\tau_w}, \quad \hat{u}_s \cdot \frac{dp}{ds} = 0, \quad (2)$$

$$A = 1, \quad \text{otherwise.} \quad (3)$$

In the equations, τ_w is the wall shear stress, $\frac{dp}{ds}$ is the stream-wise pressure gradient, \hat{u}_s is the unit vector of the local slip velocity and f is the length scale equal to the size the unresolved near-wall region. These equations are iteratively solved from the first mesh cell close to the wall in order to specify the boundary conditions of the turbulence model. For this purpose, a slip algorithm (Chen and Doolen, 1998b), obtained as generalization of a bounce-back and specular reflection process, is used.

The transient nature of the LB-VLES solutions allow the extraction of acoustic pressure in the near-field up to a cut-off frequency corresponding to approximately 15 voxels per acoustic wavelength. The acoustic

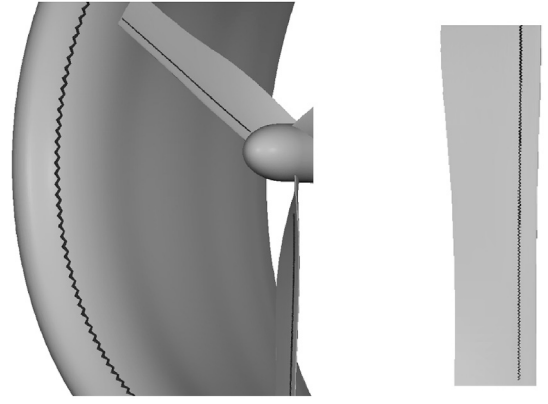


Fig. 3. Computational model showing the zig-zag trip location on the duct surface (left) and on the blade surface (right).

pressure in the far-field is computed by using the Ffowcs Williams-Hawkings (FWH) analogy (Ffowcs Williams et al., 1978). The formulation 1A developed by Farrasat with advanced-time solution (Farrasat and Succi, 1980), extended to a convective wave equation, is used in this study. Unsteady pressure fluctuations, used to compute far-field sound, are recorded on the surface of the DWT model.

3. Numerical setup

Two DWT geometries, shown in Fig. 2, with different duct cross sections (named as DonQi® and DonQi D5) are chosen. The selection is based on the duct shape optimization study conducted by the authors (Dighe et al., 2019a). The optimization procedure preserved the following geometric parameters: leading edge position (which defines the duct inlet radius R_{inlet}), trailing edge position (which defines the duct outlet radius R_{outlet}) and inner side thickness (which maintains a constant value of the clearance between the duct and the tip of the blades). It was found that the DonQi D5 duct results in power coefficient C_p improvement of approximately 5% when compared to the DonQi® duct across a wide range of AD thrust coefficients (Dighe et al., 2019a). The duct chord c is 1 m. At the inlet, $R_{inlet} = 0.87$ m, at the outlet $R_{outlet} = 1$ m and at the throat $R_{throat} = 0.77$ m. The tip clearance between the duct and the turbine blade equals 0.02 m.

Based on the previous study (Avallone et al., 2020), a baseline geometry for the wind turbine model is used. The wind turbine consists of three blades with a NACA 2207 airfoil of chord length varying from 0.13 m at the root section to 0.105 m at the tip. The blade twist angle varies from 40.5° at the root to 0.3° at the tip section. The wind turbine blades are connected to a hub (upstream) and a nacelle (downstream). The hub is composed of a cylinder, with diameter and length equal to 0.125 m and 0.1 m, respectively. Similarly, the nacelle has the cylinder length equal to 0.1 m and the diameter equal to 0.075 m.

Zig-zag trips, shown in Fig. 3, have been added to the suction sides of the duct and of the blades (Avallone et al., 2020). As shown in several wind turbine computational studies (Zhang et al., 2017; Oerlemans et al., 2007), these trips are added on turbine blades in order to force transition from laminar to turbulent flow. For the duct, an annular zig-zag trip is placed at 10% of the duct chord on the suction side. It has length, height and λ_z (i.e., tip-to-tip distance) respectively equal to 1.5 mm, 2.5 mm and 4 mm. For the blades, the zig-zag trip is placed on both the suction and the pressure side; it extends from 15% to 99% of the blade length and it has length, height and λ_z respectively equal to 0.5 mm, 1.25 mm and 4 mm. For a detailed description on the effects of zig-zag tape length, height and tip-to-tip distance, the reader can refer to the work of Anselmi (2017).

For both DWT geometries, the free-stream velocity is $U_\infty = 5$ m/s, which is a typical value for urban wind turbines, corresponding to

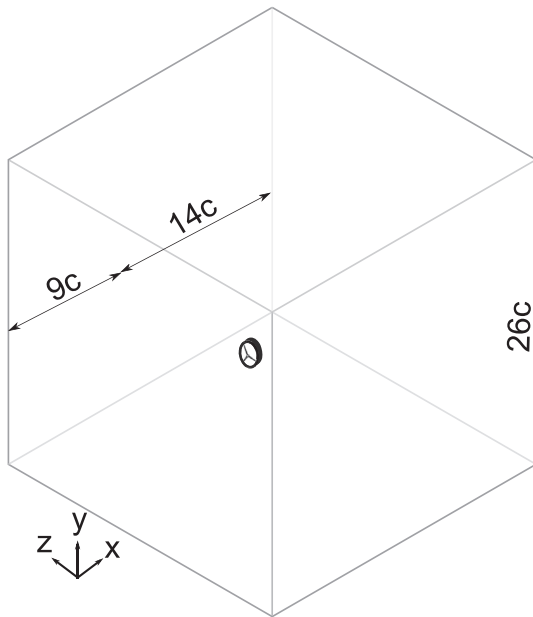


Fig. 4. Computational domain used for the LB-VLES simulations. The length are indicated in terms of duct chord length c (representative, not to scale).

Reynolds number $Re = 3.31 \times 10^5$ based on the duct chord length c . The rotational speed of the wind turbine ω is 39.84 rad/s, calculated for a tip-speed ratio $\lambda = 6$; the value is found optimal based on the previous study (Ten Hoopen, 2009). For the yawed inflow condition, DWT geometries are rotated around the center-line axis by the yaw angle $\alpha = 7.5^\circ$. The specific choice of α is based on the existing study (Anselmi, 2017) on the DonQi® DWT model and it is considered representative to show the effect of inflow yaw angle on both aerodynamic field and far-field noise. The effects of the yawed inflow conditions with different values of α on the performance of DWTs are not investigated in this paper and will be analyzed in future works.

The simulation domain is a rectangular box equal to $23c$ in the free-stream direction x , and $26c$ in the $y-z$ plane perpendicular to the flow (see Fig. 4). The DWT is located $9c$ downstream of the inlet. Free-stream velocity boundary conditions are applied at $x = -9c$ while pressure outlet boundary conditions are applied at $x = 14c$. The side walls are defined using slip boundary conditions. In total, approximately 284 million voxels and 52 million surfels are used to discretize each case. A total of 11 mesh refinement regions, named as VR, with resolution

Table 1

Voxels statistics for mesh independence study of the DWT models.

| | Coarse | Medium | Fine | Experiments |
|-------------------|--------------------|--------------------|--------------------|-------------|
| Number of voxels | 1.46×10^6 | 2.67×10^6 | 4.33×10^6 | |
| DonQi® C_{TD} | 0.410 | 0.417 | 0.419 | |
| DonQi D5 C_{TD} | 0.460 | 0.471 | 0.471 | |
| DonQi® C_T | 0.612 | 0.703 | 0.706 | 0.689 |
| DonQi D5 C_T | 0.642 | 0.723 | 0.727 | |

factor equal to 2 are employed, see Fig. 5. For simulating the rotating turbine blades within the fixed duct geometry, the three dimensional computational domain is divided into an inner and an outer domain. The inner domain has a mesh fixed with the turbine, which is specified as sliding mesh. The outer domain forms a ground-fixed domain, which does not have relative motion. The inner and outer domains are connected by a closed, zero-thickness, transparent interface. Additional details on the numerical implementation of sliding mesh, and validation examples, are given by Perot et al. (2012).

The simulation is run for 9 complete turbine revolutions, corresponding to a physical time of 1.42 s. The physical time step Δt , corresponding to a Courant–Friedrichs–Lewy (CFL) number (Courant et al., 1967) of 1 in the finest mesh refined regions is 7.27×10^{-7} s. The simulations are performed using the high-performance computing facility available at The Delft University of Technology requiring 7200 CPU hrs/revolution on a Linux Xeon E5-2690 2.9 GHz platform.

4. Validation of the numerical setup and comparison with the experiments

First, a mesh independence study is performed for the two DWT models in non-yawed inflow condition by uniformly increasing the resolution of each VR. Three resolution cases, corresponding to the smallest voxel size equal to 1200 (coarse), 1800 (medium) and 2400 (fine) voxels per duct chord, are studied. The duct thrust force coefficient C_{TD} and the total thrust force coefficient C_T for the DWT models are taken as reference for the convergence analysis. They are defined as:

$$C_{TD} = \frac{T_D}{\frac{1}{2} \rho U_\infty^2 S_{turbine}}, \quad (4)$$

$$C_T = \frac{T}{\frac{1}{2} \rho U_\infty^2 S_{exit}}, \quad (5)$$

where T_D is the duct thrust force, i.e. the axial force, generated by the

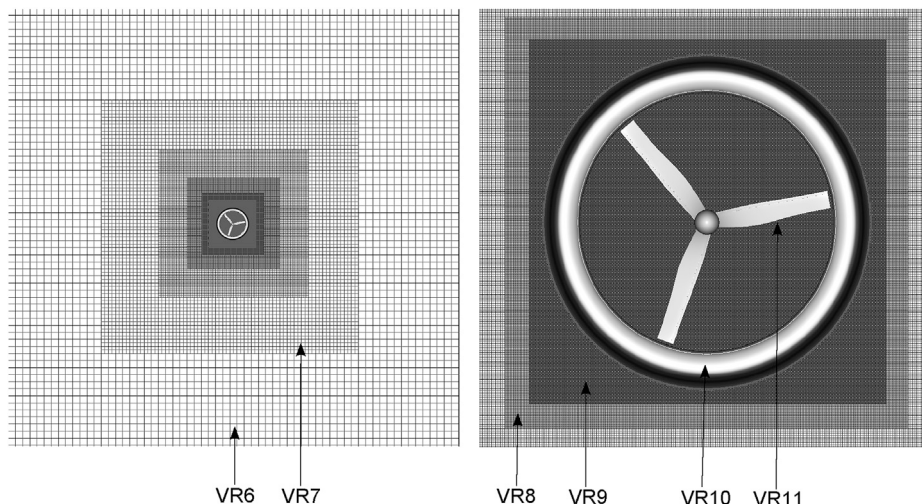


Fig. 5. Volume resolution (VR) region distribution used to discretize the DWT models showing the front view (left) and zoomed-in view (right) for the DWT model.

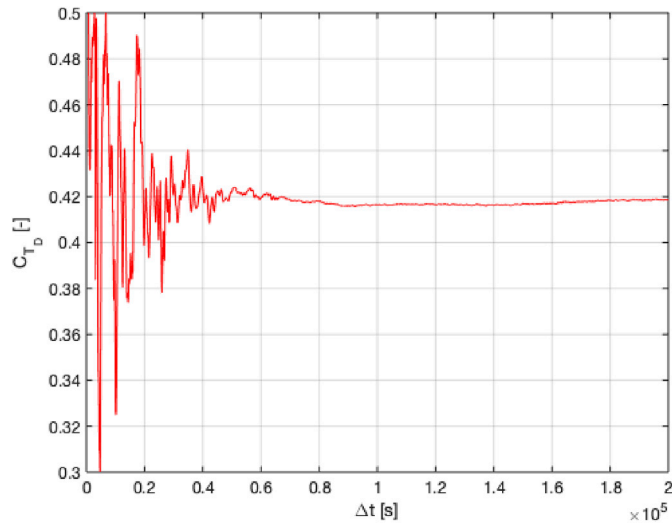


Fig. 6. Temporal convergence of C_{TD} for the DonQi® duct at zero degree yaw.

duct surface, $S_{turbine}$ is the turbine surface area equal to $\pi R_{turbine}^2$, T is the total thrust force, i.e. the axial force, generated by the DWT model and S_{exit} is the duct exit surface area equal to πR_{exit}^2 .

The results of the mesh independence study are shown in Table 1. Solution convergence is reached for the medium VR, when the observed deviations between the converged values are less than 0.5%. The medium VR mesh is then used in the rest of the paper and compared with experimental findings.

The resulting medium VR mesh is then used to assess temporal convergence, where the duct thrust force coefficient C_{TD} for the DonQi® duct at zero degree yaw is plotted against physical time step ($\Delta t = 7.27 \times 10^{-7}$ s) in Fig. 6. After two turbine rotations, i.e. $\approx 0.5 \times 10^5$ s, the C_{TD} value reached a quasi-steady state, thus indicating temporally converged solution.

As further validation of the numerical approach, numerical results are compared with the experimental ones reported by Ten Hoopen (2017) who investigated experimentally the DonQi® DWT model in non-yawed inflow condition (see Fig. 7). Experiments were conducted in the closed-loop open-jet (OJF) wind tunnel facility at the Delft University of Technology. During the experiments, the free-stream turbulence intensity, T_i of 0.21%, was measured at the turbine blade location. Transition was not forced but the experimental model has a noise damper, see Fig. 7, which acts as rough surface that forces transition to turbulence; this has not been replicated numerically. Ten Hoopen measured the total thrust force exerted by the DonQi® DWT model using an axial force balance system. The C_T calculated from the wind tunnel measurements is 0.689 while by CFD it is 0.703; see Table 1. The numerical and experimental results differ by 2%, which is within the experimental uncertainty.

The duct surface pressure distribution, measured in the experiments using pressure taps arranged along the duct chord length, is compared with the numerical one in Fig. 8. In the figure, the duct surface pressure coefficient c_p is plotted as a function of normalized duct chord length x/c . Results from CFD are obtained by azimuthally averaging the c_p values over two complete turbine rotations after reaching temporal convergence. Overall, a very good agreement for the c_p values between the CFD data and the experimental results is found. The deviation at $x/c = 2$ is due to the presence of noise damper (see Fig. 7) in the experimental model which is not included in the numerical model.

5. Flow-field analysis

The instantaneous flow fields around the two DWTs, both in non-yawed and yawed inflow conditions, are shown in Fig. 9 (a)-(d) using



Fig. 7. Front view of the DonQi® DWT model used for the experimental study (Ten Hoopen, 2017).

the λ_2 criterion for vortex identification (Jeong and Hussain, 1995) color-contoured with the normalized streamwise velocity magnitude.

For the DonQi® configuration at $\alpha = 0^\circ$, as in Fig. 9(a), tip vortices convecting over the inner walls of the duct are clearly visible. These vortices, convect in the duct following a helicoidal pattern, become unstable and break up in smaller structures towards the exit plane of the duct (Avalone et al., 2020). By increasing the camber of the duct cross section, as in Fig. 9 (b), a larger flow acceleration is present along the suction side of the duct. This has an effect on the local boundary layer thickness at the turbine plane, thus changing the ratio between the tip-clearance and the boundary layer thickness. In this case, the boundary layer thickness is thicker than that observed for the baseline case, and, as a consequence, the tip vortex breaks at the turbine plane with generation of turbulent flow structures along the duct inner walls. A similar phenomenon was observed in a previous study by Avalone et al. (2020) on the baseline DWT geometry by changing the tip-clearance of the blades. Focusing on the duct pressure side, large coherent structures are formed at the leading edge of the DonQi D5 model, which convect and break into smaller ones at more downstream locations. This is caused by the fact that the curvature of the DonQi D5 airfoil is larger than the one of the baseline duct and transition to turbulence is anticipated.

By introducing a yaw angle, as in Fig. 9(c) and (d), the flow fields, for both configurations, show differences in the turbulent flow structures convecting over the inner walls of the duct. A major difference between the two configurations is that, for the baseline configuration, the tip vortex is generated at the turbine plane and interact with the duct surface at downstream locations where it breaks in smaller structures. Differently, for the DonQi D5 configuration, as for the case with zero yaw angle, the tip vortex breaks at the turbine plane. For this case, the flow is richer of turbulent flow structures, and it decelerates just downstream of the turbine plane as visible from the blue contour representing normalized streamwise velocity component. For this particular case, the yawed inflow causes an early breakdown of the main vortex into smaller structures on the pressure side of the duct.

To better show the aerodynamic interactions between the near wake of the turbine and the turbulent boundary layer convecting over the duct surface, 2D visualization in the x - y plane of the instantaneous flow fields are shown in Fig. 10 (a)-(d). As in the previous figures, non-dimensional contours of the streamwise velocity components U_x/U_∞ are plotted.

For all the cases, it can be observed that, as expected, the velocity at the turbine plane is higher than the free-stream velocity. As discussed in the introduction, this is due to the airfoil-shaped duct, which acts as a

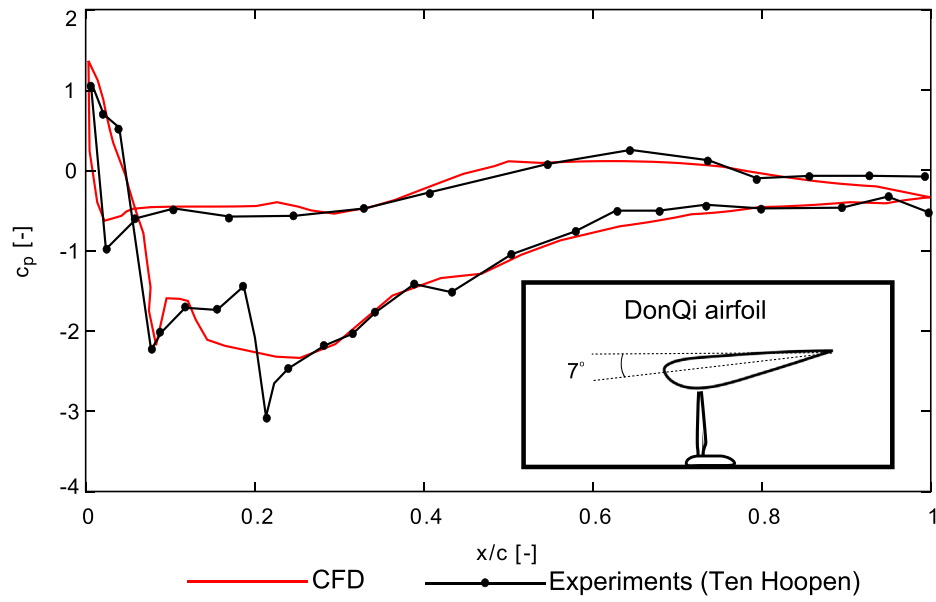


Fig. 8. Comparison of duct surface pressure coefficient c_p between the experimental data and the CFD findings shown for DonQi® DWT model in non-yawed inflow condition.

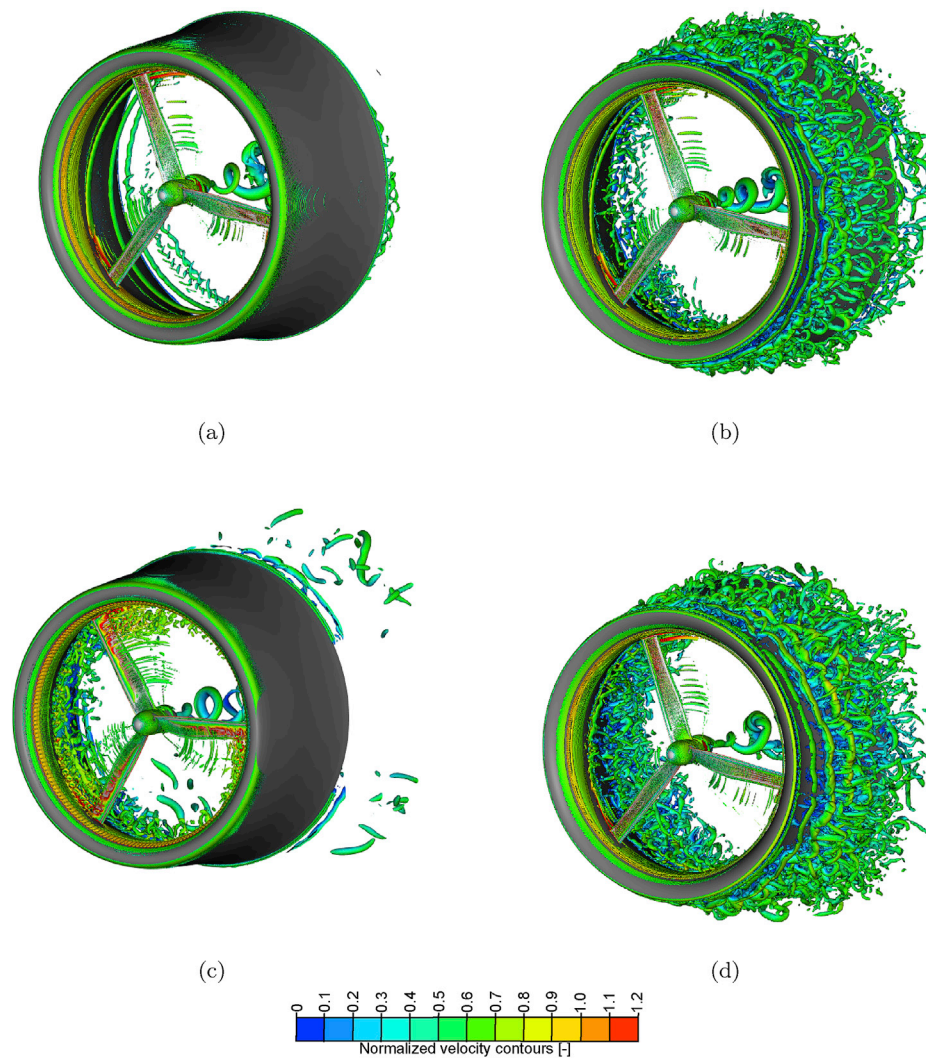


Fig. 9. Visualization of the instantaneous flow fields using iso-surface of the λ_2 criterion for vortex identification colored-contoured with normalized streamwise velocity component U_x/U_∞ for (a) DonQi® model at $\alpha = 0^\circ$, (b) DonQi D5 model at $\alpha = 0^\circ$, (c) DonQi® model at $\alpha = 7.5^\circ$ and (d) DonQi D5 model at $\alpha = 7.5^\circ$.

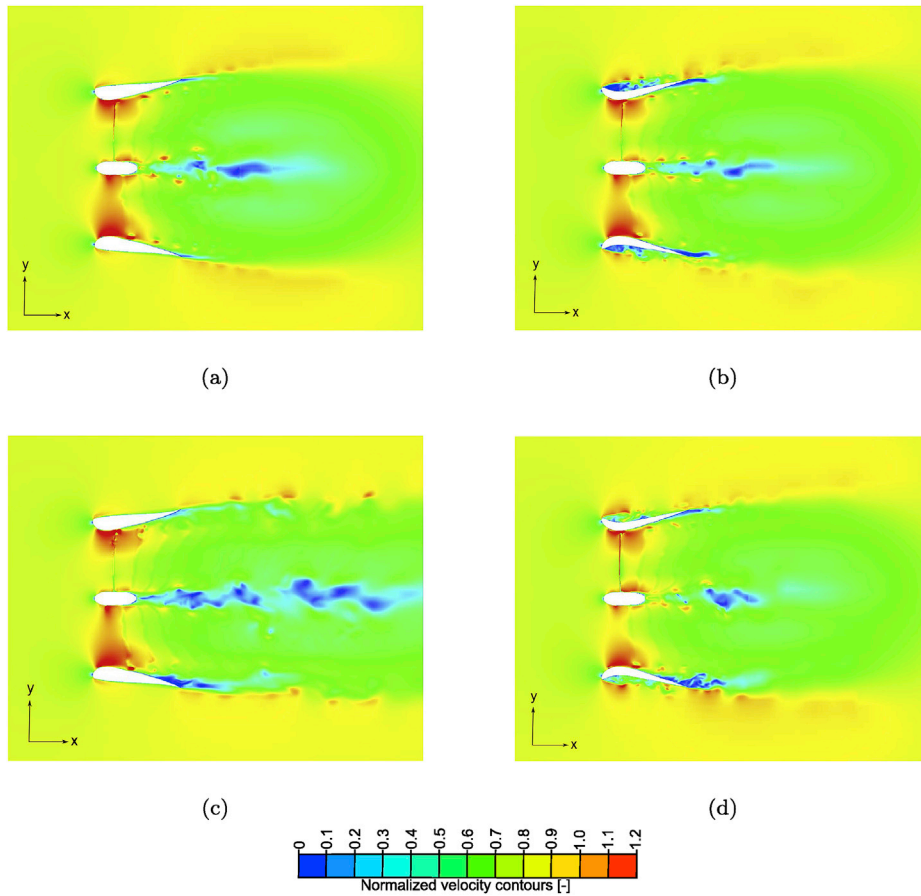


Fig. 10. Contours of instantaneous streamwise velocity U_x/U_∞ in the $x - y$ plane for (a) DonQi® at $\alpha = 0^\circ$, (b) DonQi D5 at $\alpha = 0^\circ$, (c) DonQi® at $\alpha = 7.5^\circ$ and (d) DonQi D5 at $\alpha = 7.5^\circ$.

convergent-divergent nozzle that accelerates the flow (i.e., increases the mass-flow rate). The velocity in the plane of rotation varies in the radial direction with the maximum velocity observed towards the tip region of the turbine blade (Avallone et al., 2020). Here, the tip gap between the duct and turbine accelerates the flow via a mechanism similar to boundary layer blowing (Avallone et al., 2020; Kwong and Dowling,

1994).

For the baseline DonQi® model at zero degree yaw angle (Fig. 10 (a)), the flow over the suction side of the duct (i.e., the inner wall) weakly separates at about the 95% of the duct chord length. This is visualized by the low velocity region close to the trailing edge. For the same inflow condition, the DonQi D5 model shows earlier flow separation starting

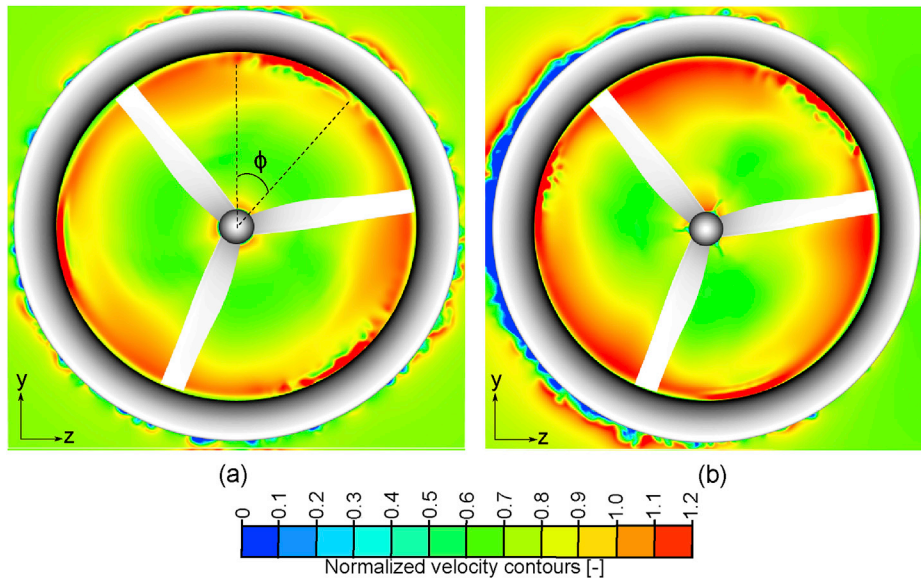
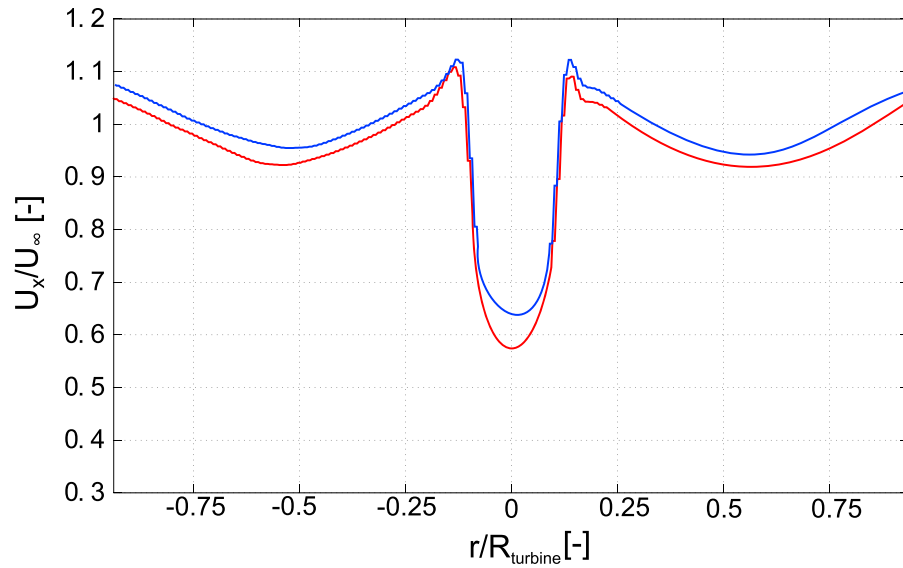
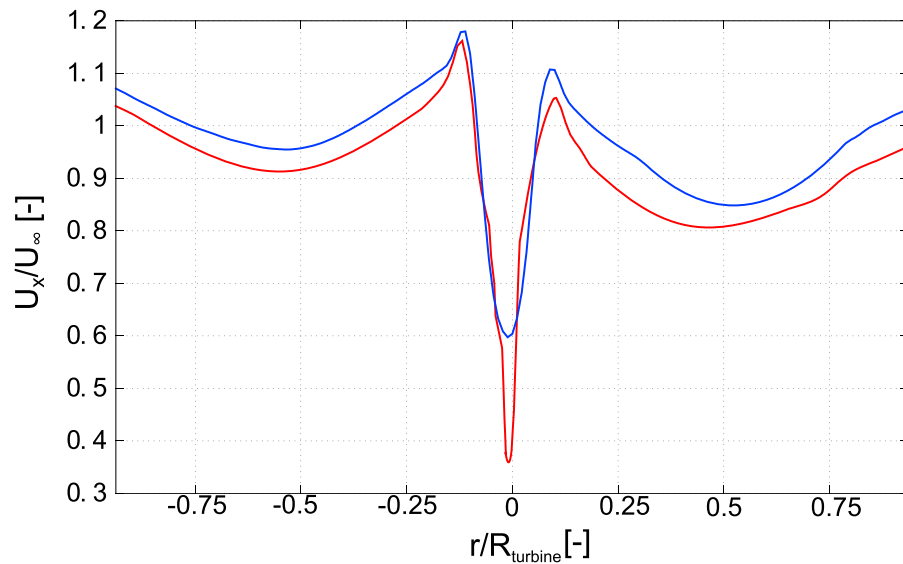


Fig. 11. Contours of instantaneous streamwise velocity U_x/U_∞ in the $y - z$ plane for DonQi D5 in (a) non-yawed and (b) yawed inflow condition.



(a)



(b)

————— DonQi[®]
————— DonQi D5

Fig. 12. Radial distribution of azimuthally averaged streamwise velocity U_x/U_∞ measured at the turbine plane.

from 85% of the duct chord length over the suction side (Fig. 10 (b)). For this particular case, the velocity slows down on the pressure side of the duct due to the airfoil curvature. As a result, pressure drops on the suction side of the duct and increased mass flow is swallowed by the turbine as explained by Dighe et al. (2019a). Fig. 10(a) and (b) give further insights on the breaking up process of the tip vortex in smaller vortical structures. For the baseline configuration, there is a weak interaction between the boundary layer convecting over the inner walls of the duct and the tip vortex. As a matter of fact, footprints of the tip vortices are clearly visible within the duct. For the DonQi D5 model, the footprints of the vortices are weaker since they interact with the separated boundary layer.

The baseline configuration with yawed inflow (Fig. 10 (c)) shows that flow separation moves upstream; the resulting thicker boundary layer

interacts with the tip vortex thus breaking up in smaller structures. These velocity fluctuations in the near wake resembles the vortex dynamics breakdown for HAWTs in yaw, thus reducing the overall thrust generated by the turbine blades (Jiménez et al., 2010). For the DonQi D5 model in yawed inflow (Fig. 10 (d)), the separation location within the duct weakly changes with respect to the zero-yaw configuration (Fig. 10 (b)).

Fig. 11 shows instantaneous contours of U_x/U_∞ in the $y-z$ plane at the turbine location for the DonQi D5 model in non-yawed (Fig. 11 (a)) and yawed (Fig. 11 (b)) inflow conditions. The presence of a yaw angle causes an asymmetric flow field, thus the velocity at the turbine plane changes with the azimuthal angle Φ . Here, the azimuthal angle Φ is defined as rotating clockwise when looking upwind, with zero aligned in the positive y direction (see Fig. 11 (a)). The figure highlights the higher

Table 2
Aerodynamic performance coefficients for the two DWT models.

| | DonQi | | DonQi D5 | |
|---------------|--------|--------|----------|--------|
| | 0° | 7.5° | 0° | 7.5° |
| C_{TD} | 0.4238 | 0.3587 | 0.4812 | 0.5014 |
| $C_{Turbine}$ | 0.8292 | 0.7170 | 0.8417 | 0.8803 |
| C_p | 0.7545 | 0.6309 | 0.7675 | 0.7922 |
| C_{Pexit} | 0.4244 | 0.3549 | 0.4317 | 0.4566 |

velocity at the turbine plane for the yawed inflow configuration. This is quantified by plotting the azimuthally averaged streamwise velocity component in the radial direction ($r/R_{turbine}$) in Fig. 12. The DWT with larger camber cross-section airfoil, shows an increase of U_x/U_∞ of about 5% along the entire radius for the zero-yaw configuration and of about 10% for the 7.5° yaw angle. More interesting, the DWT with higher camber duct is less affected by the yaw angle than the baseline one. Finally, as expected, because of the yaw angle, the time-averaged velocity distribution is asymmetric. This can cause unsteady loading generation, that can induce unsteady forces on the system, thus increasing the possibility of mechanical failures.

6. Aerodynamic performance

Table 2 summarizes the aerodynamic performance coefficients for both DWT models calculated under non-yawed and yawed inflow conditions. The duct thrust force coefficient C_{TD} , turbine thrust force coefficient $C_{Turbine}$ and power coefficient C_p are shown. The values are obtained as time average over two complete turbine rotations after reaching temporal convergence.

The duct thrust force coefficient C_{TD} is defined in equation (4). The turbine thrust force coefficient $C_{Turbine}$ is defined as:

$$C_{Turbine} = \frac{T_{turbine}}{\frac{1}{2}\rho U_\infty^2 S_{turbine}}, \quad (6)$$

where $T_{turbine}$ is the turbine thrust force, i.e. the axial thrust force, generated by the turbine blades, and $S_{turbine}$ is the turbine surface area equal to $\pi R_{turbine}^2$.

The power coefficient C_p , expressed as a function of turbine thrust force coefficient $C_{Turbine}$ and the azimuthally averaged surface integral of the axial velocity distribution U_x/U_∞ along the turbine's plane of rotation (from Fig. 12), is given by:

$$C_p = \frac{P}{\frac{1}{2}\rho U_\infty^3 S_{turbine}} = C_{Turbine} \int_{S_{turbine}} \frac{U_x}{U_\infty}. \quad (7)$$

It is worth mentioning that some studies adopt a different definition for the power coefficient of a DWT in which the reference area is taken at the duct exit section (van Bussel, 2007), given by:

$$C_{Pexit} = \frac{P}{\frac{1}{2}\rho U_\infty^3 S_{exit}}. \quad (8)$$

As a result, the power coefficient C_{Pexit} obtained is smaller than the one obtained using C_p . So that, with the help of reference areas S_{AD} and S_{exit} , the difference in the power coefficients can be expressed as:

$$\frac{C_p}{C_{Pexit}} = \frac{S_{exit}}{S_{AD}}. \quad (9)$$

For the current study, C_p is used. However, the C_{Pexit} calculated for the two DWT models under different inflow conditions are shown in Table 2 for the sake of completeness. The C_p values calculated for the DWT models challenges the well-known Lanchester–Betz–Joukowsky limit of $C_p = 0.593$ as maximum power coefficient obtainable for HAWTs (van Kuik, 2007). This should not appear like a surprising result, since, the mass flow of air swallowed in the presence of duct is larger (see Fig. 10

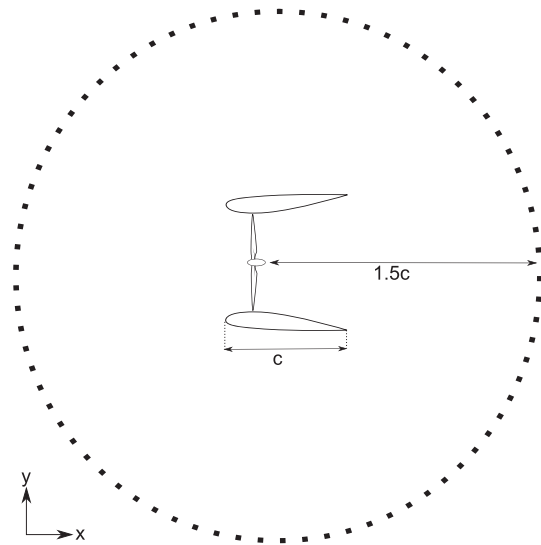


Fig. 13. Schematic showing 72 microphones positioned at $1.5c$ from the center of the DWT and normal to the plane of turbine rotation.

(a)–(d) due to the additional thrust force C_{TD} offered by the duct. Dighe et al. (2019a) concluded that for a given turbine configuration, the C_p of a DWT can be increased if and only if C_{TD} is increased. Then, if C_{TD} increases, $C_{Turbine}$ and ultimately C_p also increase, coherently to what is observed in Table 2. The comparison of the aerodynamic performance coefficients of the two DWT models in Table 2 shows that, for the same duct exit area, the DonQi D5 model outperforms DonQi® model, both in non-yawed and yawed inflow conditions. The performance improvement for the DonQi D5 model can be attributed to the duct profile camber, which enhances C_{TD} .

For the DonQi® model at $\alpha = 7.5^\circ$, C_{TD} returns a lower value in comparison to the C_{TD} at $\alpha = 0^\circ$. As a consequence, $C_{Turbine}$ and C_p calculated at $\alpha = 7.5^\circ$ is lower by 13.5% and 16.4% respectively than that calculated at $\alpha = 0^\circ$. Contrariwise, for the DonQi D5 model, C_{TD} at $\alpha = 7.5^\circ$ is higher than that obtained at $\alpha = 0^\circ$. As explained before, this is because the duct camber increases the C_{TD} in yawed inflow conditions, as also noted in 2D simulation by Dighe et al., 2019. Then, the $C_{Turbine}$ and C_p calculated at $\alpha = 7.5^\circ$ is higher by 4.4% and 3.2% respectively than that calculated at $\alpha = 0^\circ$ for the DonQi D5 model.

7. Noise estimation

The effect of the duct geometry and inflow conditions on the acoustic behavior of the two DWT models is investigated in this section. Noise is estimated on a circular array of 72 equally spaced microphones in the $x - y$ plane placed at $1.5c$ from the plane of rotation (Fig. 13).

Fig. 14(a) and (b) show the Overall Sound Pressure Level (OASPL) expressed in decibel (dB) with reference pressure equal to 20×10^{-6} Pa. Results are integrated from 2 Hz to 392.4 Hz, i.e. up to 20 times the Blade Passing Frequency (BPF). It can be observed that the OASPL generated by the DonQi D5 model is higher than that of the DonQi® one, both in non-yawed and yawed inflow conditions. Starting with the non-yawed inflow (Fig. 14 (a)), differences in the OASPL directivity patterns are observed; they are localized in certain flow directions, i.e. in the axial direction upstream of the DWT and at $\pm 120^\circ$. At these locations, the DonQi D5 model is approximately 15 dB and 20 dB louder than the baseline configuration. For the yawed inflow configuration (Fig. 14 (b)), the directivity plots are similar in shape to the zero-yaw angle case but tilted. The asymmetric OASPL directivity, for the yawed inflow case, is caused by the asymmetric nature of the inflow velocity (Fig. 12) and of the consequent turbulent flow at the trailing edge of the duct (Fig. 10).

The shape of the directivity plots for the DonQi D5 model, both in

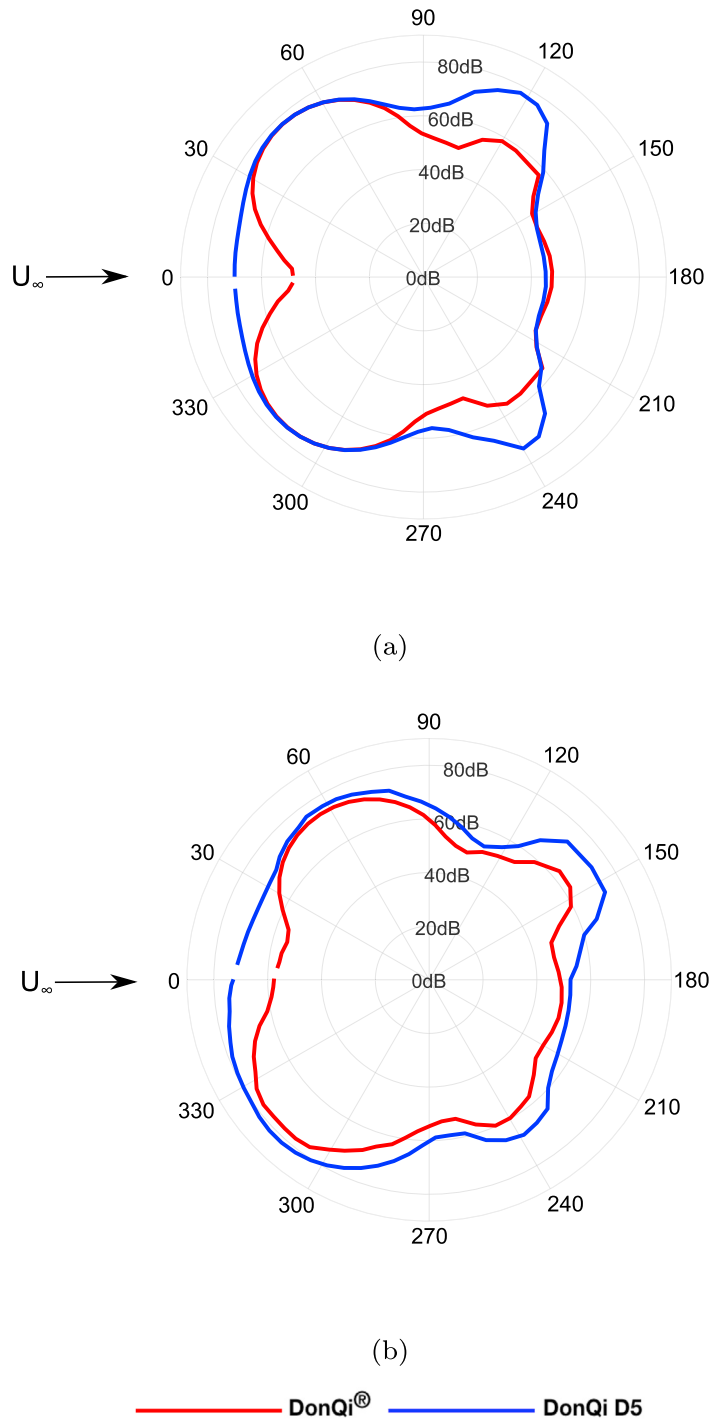
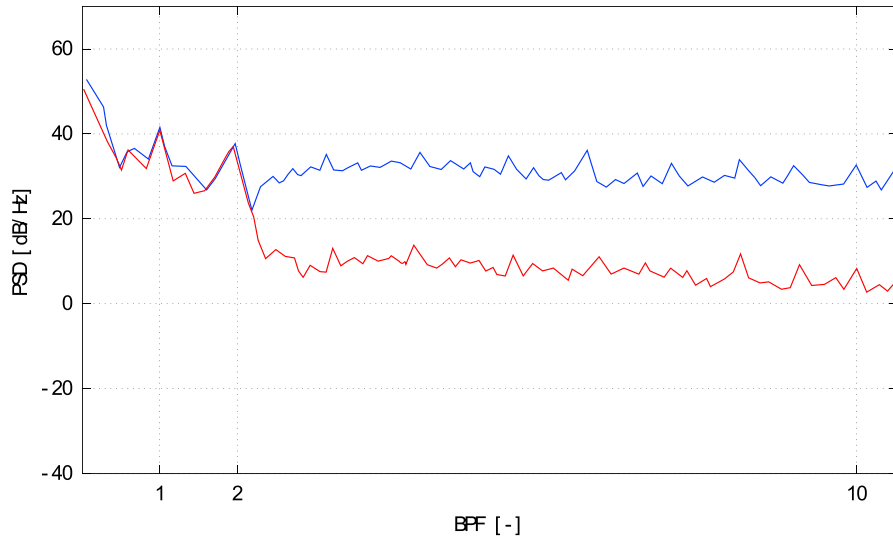


Fig. 14. Overall Sound Pressure Level (OASPL) obtained for the two DWT models in (a) non-yawed inflow condition and (b) yawed inflow condition.

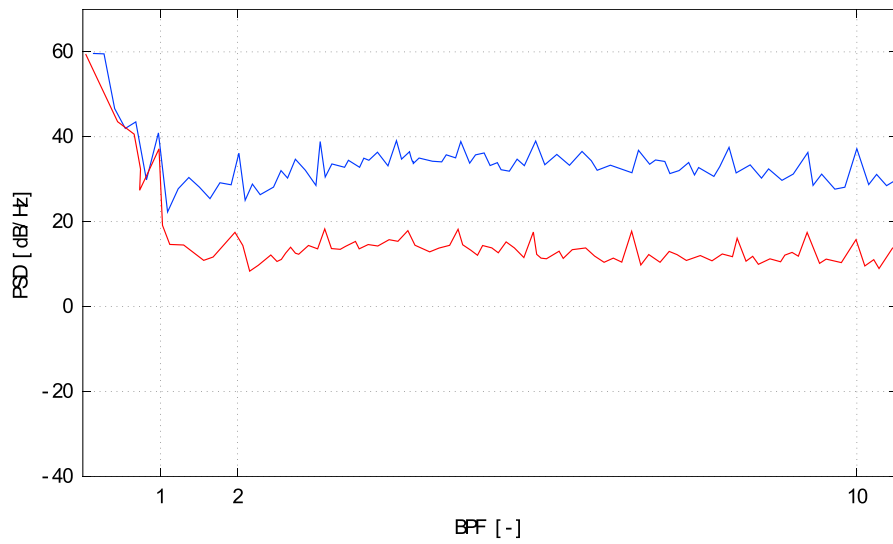
non-yawed and yawed inflow conditions, show the appearance of larger lobes in the downstream direction in comparison to the baseline case. This can be associated to turbulent boundary layer trailing edge noise caused by the turbulent flow structures convecting along the duct (Brooks et al., 1989), as shown previously in Fig. 9. Noise increase in the axial direction is instead related to the variation of the local boundary layer thickness at the turbine plane, and due to the presence of an additional noise source related to flow instabilities as found by Avallone et al. (2020).

To further explore the presence of an additional source of noise

related to turbulent boundary layer trailing edge noise, Power Spectral Density (PSD) plots versus the blade Passing Frequency (BPF), expressed in dB/Hz, are shown for a microphone located at 90° with respect to the free-stream direction in Fig. 15. For the non-yawed inflow condition, at frequencies higher than 2 BPF, the PSD curves diverges; the DonQi D5 model shows larger broadband noise with amplitude almost equal to the tonal peak at the 2nd BPF. For the yaw angle case, the PSD curves are almost identical up to the 1st BPF. Beyond this frequency, broadband noise dominates and becomes comparable to the tonal peak at the 1st BPF. The increase of the broadband noise component also for the baseline



(a)



(b)

— DonQi® — DonQi D5

Fig. 15. Power Spectral Density (PSD) versus the Blade Passing Frequency (BPF) for a microphone located at 90° under (a) non-yawed inflow condition and (b) yawed inflow condition.

configuration at yaw angle confirms that the additional noise is related to turbulent boundary layer trailing edge noise.

8. Conclusions

In this work, the aerodynamic and aeroacoustic performances of DWTs, both in non-yawed ($\alpha = 0^\circ$) and yawed ($\alpha = 7.5^\circ$) inflow conditions, are investigated. To this aim, three-dimensional numerical calculations using Lattice-Boltzmann Very-Large-Eddy Simulations (LB-VLES) are carried out. To validate the numerical approach, emphasis has been given to the comparison of CFD results with the experiments. Based on a previous study conducted by the authors (Dighe et al., 2019a), two DWT models (DonQi® and DonQi D5) are chosen. The geometric parameters of the DWT models are identical, except for the duct geometry, which have

different cross-section camber.

The analysis shows the possibility to significantly increase the DWTs aerodynamic performance by increasing the duct profile camber, whilst maintaining the same duct exit area ratio. Comparing the two DWT models, the power coefficient C_P for the DonQi D5 DWT model is approximately 1.7% and 20.4% higher than the DonQi® DWT model in non-yawed and yawed inflow conditions, respectively. More interestingly, DonQi D5 DWT model is less affected by the yaw inflow angle and a gain in the C_P by approximately 3% is obtained. Future studies will investigate up to which yaw angle this beneficial effect holds. The aerodynamic performance improvement, in terms of the turbine thrust force coefficient $C_{T_{turbine}}$ and C_P , for a DWT model corresponds to the increase of the duct thrust force coefficient C_{TD} . Velocity contours shows that the cambered airfoil improves the yaw insensitivity for the DWT

model because it guarantees a higher velocity magnitude and slightly less asymmetric velocity profile at the rotor plane with respect to the baseline configuration. The yaw insensitivity for the DWT model, however, strongly depends on the aerodynamic mutual interactions between the duct and turbine, which may change by varying the duct geometry, turbine configuration and yaw angle.

The duct shape has a strong effect on the noise. The overall sound pressure level (OASPL) is calculated at a circular array of microphones normal to the plane of rotation. The highly cambered configuration (DonQi D5 model) is approximately 10–15 dB louder than the baseline one (DonQi® model), both in non-yawed and yawed inflow conditions. Power spectral density (PSD) analysis shows that the broadband noise contribution becomes higher for the DonQi D5 model in comparison to the DonQi® model, both in non-yawed and yawed inflow conditions. The additional broadband noise source is due to turbulent boundary layer trailing edge noise due to the turbulent flow structures developing along the surface of the duct. This source of noise can be mitigated with the installation of trailing edge serrations (Avallone et al., 2018, 2017) or porous materials (Rubio Carpio et al., 2019).

Declaration of competing interest

The authors declare that they have no known competing financial interests or personal relationships that could have appeared to influence the work reported in this paper.

CRediT authorship contribution statement

Vinit V. Dighe: Conceptualization, Methodology, Software, Validation, Formal analysis, Investigation, Visualization. **Francesco Avallone:** Supervision, Investigation. **Gerard van Bussel:** Supervision, Project administration, Funding acquisition.

Acknowledgement

The research is supported by STW organization, grant number-12728.

References

- Anselmi, L., 2017. Computational analysis of ducted wind turbines noise. TU Delft Repos. 32, 32–39.
- Avallone, F., van der Velden, W., Ragni, D., 2017. Benefits of curved serrations on broadband trailing-edge noise reduction. *J. Sound Vib.* 400, 167–177.
- Avallone, F., Van Der Velden, W., Ragni, D., Casalino, D., 2018. Noise reduction mechanisms of sawtooth and combed-sawtooth trailing-edge serrations. *J. Fluid Mech.* 848 <https://doi.org/10.1017/jfm.2018.377>.
- Avallone, F., Ragni, D., Casalino, D., 2020. On the effect of the tip-clearance ratio on the aeroacoustics of a diffuser-augmented wind turbine. *Renew. Energy* 152, 1317–1327. <https://doi.org/10.1016/j.renene.2020.01.064>.
- Barthelme, R., Pryor, S., 2014. Potential contribution of wind energy to climate change mitigation. *Nat. Clim. Change* 4 (8), 684.
- Bontempo, R., Manna, M., 2013. Solution of the flow over a non-uniform heavily loaded ducted actuator disk. *J. Fluid Mech.* 728, 163–195.
- Brooks, T., Pope, D., Marcolini, M., 1989. Airfoil Self-Noise and Prediction. Technical Report.
- Chen, S., Doolen, G.D., 1998a. Lattice Boltzmann method for fluid flows. *Annu. Rev. Fluid Mech.* 30 (1), 329–364.
- Chen, S., Doolen, G.D., 1998b. Lattice Boltzmann method for fluid flows. *Annu. Rev. Fluid Mech.* 30 (1), 329–364.
- Courant, R., Friedrichs, K., Lewy, H., 1967. On the partial difference equations of mathematical physics. *IBM J. Res. Dev.* 11 (2), 215–234.
- De Oliveira, G., Pereira, R., Ragni, D., Avallone, F., Van Bussel, G., 2016. How does the presence of a body affect the performance of an actuator disk?. In: *Journal of Physics: Conference Series*, vol. 753. IOP Publishing, p. 022005.
- de Vries, O., 1979. Fluid Dynamic Aspects of Wind Energy Conversion. Advisory Group for Aerospace Research and Development NEUILLY-SUR-SEINE (France). Technical Report.
- Dighe, V., de Oliveira, G., Avallone, F., van Bussel, G., 2019a. Characterization of aerodynamic performance of ducted wind turbines: a numerical study. *Wind Energy* 1037 (2), 022–016.
- Dighe, V., Suri, D., Avallone, F., van Bussel, G., 2019b. Ducted wind turbines in yawed flow: a numerical study. *Wind Energy Sci. Dis.* 2019, 1–13.
- Farassat, F., Succi, G.P., 1980. A review of propeller discrete frequency noise prediction technology with emphasis on two current methods for time domain calculations. *J. Sound Vib.* 71 (3), 399–419.
- Ffowcs Williams, J., Dowling, A.P., Goldstein, M.E., 1978. Sound production in a moving stream. *Phil. Trans. Roy. Soc. Lond. Math. Phys. Sci.* 288 (1353), 321–349.
- Fogaing, M.B.T., Gordon, H., Lange, C.F., Wood, D.H., Fleck, B.A., 2019. A review of wind energy resource assessment in the urban environment. *Adv. Sustain. Energy* 7–36.
- Foreman, K.M., Gilbert, B.L., 1984. Diffuser for Augmenting a Wind Turbine. US Patent, 4482290A.
- Gilbert, B., Foreman, K., 1983. Experiments with a diffuser-augmented model wind turbine. *J. Energy Resour. Technol.* 105 (1), 46–53.
- Hansen, M.O.L., Sørensen, N.N., Flay, R., 2000. Effect of placing a diffuser around a wind turbine. *Wind Energy: Int. J. Prog. Appl. Wind Power Convers. Technol.* 3 (4), 207–213.
- Igra, O., 1976. Shrouds for aerogenerators. *AIAA J.* 14 (10), 1481–1483.
- Igra, O., 1977. Compact shrouds for wind turbines. *Energy Convers.* 16 (4), 149–157.
- Igra, O., 1981. Research and development for shrouded wind turbines. *Energy Convers. Manag.* 21 (1), 13–48.
- Jamieson, P., Hassan, G., 2011. *Innovation in Wind Turbine Design*, Volume 2. Wiley Online Library.
- Jeong, J., Hussain, F., 1995. On the identification of a vortex. *J. Fluid Mech.* 285, 69–94.
- Jiménez, Á., Crespo, A., Migoya, E., 2010. Application of a les technique to characterize the wake deflection of a wind turbine in yaw. *Wind Energy* 13 (6), 559–572.
- Kogan, A., Nissim, E., 1962. Design and Performance of a Shrouded Windmill for Power Generation. Technion-Israel Institute of Technology, Department of Aeronautical Engineering.
- Kogan, A., Seginer, A., 1963. Shrouded Aerogenerator Design Study: II. Axisymmetrical Shroud Performance. Technion-Israel Institute of Technology, Department of Aeronautical Engineering.
- Kwong, A.H., Dowling, A.P., 1994. Active boundary-layer control in diffusers. *AIAA J.* 32 (12), 2409–2414.
- Lauder, B.E., Sharma, B., 1974. Application of the energy-dissipation model of turbulence to the calculation of flow near a spinning disc. *Lett. Heat Mass Tran.* 1 (2), 131–137.
- Lilley, G., Rainbird, W., 1956. A Preliminary Report on the Design and Performance of Ducted Windmills. Technical Report. College of Aeronautics Cranfield.
- Lubitz, W.D., Shomer, A., 2014. Wind loads and efficiency of a diffuser augmented wind turbine (dawt). In: *Proceedings of the Canadian Society for Mechanical Engineering International Congress*, pp. 1–5.
- Oerlemans, S., Sijtsma, P., López, B.M., 2007. Location and quantification of noise sources on a wind turbine. *J. Sound Vib.* 299 (4–5), 869–883.
- Ohya, Y., Karasudani, T., 2010. A shrouded wind turbine generating high output power with wind-lens technology. *Energies* 3 (4), 634–649.
- Perot, F., Kim, M.S., Meskine, M., 2012. Nrel wind turbine aerodynamics validation and noise predictions using a lattice Boltzmann method. In: *18th AIAA/CEAS Aeroacoustics Conference (33rd AIAA Aeroacoustics Conference)*, p. 2290.
- Phillips, D., Flay, R., Nash, T., et al., 1999. Aerodynamic analysis and monitoring of the vortec 7 diffuser-augmented wind turbine. *Trans. Inst. Prof. Eng. N. Z. Electr. Mech. Chem. Eng.* 26 (1), 13.
- Phillips, D., Richards, P., Flay, R., 2008. Diffuser Development for a Diffuser Augmented Wind Turbine Using Computational Fluid Dynamics. Department of Mechanical, Engineering, the University of Auckland, New Zealand.
- Rubio Carpio, A., Merino-Martínez, R., Avallone, F., Ragni, D., Snellen, M., van der Zwaag, S., 2019. Experimental characterization of the turbulent boundary layer over a porous trailing edge for noise abatement. *J. Sound Vib.* 443, 537–558.
- Shan, X., Yuan, X.F., Chen, H., 2006. Kinetic theory representation of hydrodynamics: a way beyond the Navier–Stokes equation. *J. Fluid Mech.* 550, 413–441.
- Succi, S., 2001. *The Lattice Boltzmann Equation: for Fluid Dynamics and beyond*. Oxford university press.
- Takahashi, S., Hata, Y., Ohya, Y., Karasudani, T., Uchida, T., 2012. Behavior of the blade tip vortices of a wind turbine equipped with a brimmed-diffuser shroud. *Energies* 5 (12), 5229–5242.
- Teixeira, C.M., 1998. Incorporating turbulence models into the lattice-Boltzmann method. *Int. J. Mod. Phys. C* 9 (8), 1159–1175.
- Ten Hoopen, P., 2009. An Experimental and Computational Investigation of a Diffuser Augmented Wind Turbine. Ph.D. thesis; Thesis, M. Sc. Thesis. Delft University of Technology, Delft, The Netherlands.
- Ten Hoopen, P., 2017. An experimental and computational investigation of a diffuser augmented wind turbine with an application of vortex generators on the diffuser trailing edge. TU Delft Repos. 16, 35–39.
- van Bussel, G., 2007. The science of making more torque from wind: diffuser experiments and theory revisited. *J. Phys. Conf.* 75 (1), 120–10.
- van Bussel, G., 2015. Duct4U - Ducted Wind Turbine Optimi-Sation and Utilisation. Technical Report. Open Technology Programme - STW.
- van Kuik, G.A., 2007. The lanchester–betz–joukowski limit. *Wind Energy: Int. J. Prog. Appl. Wind Power Convers. Technol.* 10 (3), 289–291.
- Werle, M.J., Presz Jr., W.M., 2009. Shroud and ejector augmenters for subsonic propulsion and power systems. *J. Propul. Power* 25 (1), 228–236.
- Widnall, S., 2009. Potential Flow Calculations of Axisymmetric Ducted Wind Turbines.
- Zhang, Y., van Zuijlen, A., van Bussel, G., 2017. The Mexico rotor aerodynamic loads prediction: zigzag tape effects and laminar-turbulent transition modeling in CFD. *J. Wind Eng. Ind. Aerod.* 168, 152–163.